JID: PROCI

ARTICLE IN PRESS [mNS;July 22, 2022;20:25]

Available online at www.sciencedirect.com

ScienceDirect

Proceedings
of the
Combustion
Institute

Proceedings of the Combustion Institute 000 (2022) 1-11

www.elsevier.com/locate/proci

Vortex breakdown in swirling Burke–Schumann flames

Benjamin W. Keeton*, Keiko K. Nomura, Antonio L. Sánchez, Forman A. Williams

Department of Mechanical and Aerospace Engineering, University of California San Diego, La Jolla, CA 92093-0411, USA

Received 5 January 2022; accepted 2 July 2022 Available online xxx

Abstract

Unsteady axisymmetric numerical simulations are used to determine the transition to bubble and conical vortex breakdown in low-Mach-number laminar swirling Burke–Schumann flames, for which an ambient-temperature fuel jet in solid-body rotation emerges into quiescent air. A critical value of the swirl number S for the onset of the bubble (S_B^*) and the cone (S_C^*) is determined as the jet fuel-feed mass fraction $Y_{F,j}$ is varied for fixed Re = 800, assuming typical conditions for methane combustion with air. During the first transition from pre-breakdown to the bubble, the jet core is relatively unaffected by the flame in the surrounding shear layer, and $S_B^* = 1.36$ is constant for all values of dilution. This transition to the jet-like bubble breakdown flame is found to be in agreement with theoretical predictions based on the criterion of failure of the slender quasicylindrical approximation. Variation in the critical swirl number S_C^* , characterizing the second transition from the bubble to the cone, is relatively small ($1.80 \le S_C^* \le 1.83$) in the range $0.1 \le Y_{F,j} \le 1$, but the resulting flow and flame shape for conical breakdown is found to depend critically on $Y_{F,j}$. For realistic values of dilution ($Y_{F,j} \ge 0.2$), the bubble transitions to a steady compact cone at S_C^* with a flame sheet that passes around the recirculation region, maintaining a jet-like flame. In the extreme dilution case ($Y_{F,j} = 0.1$), the reaction sheet occurs closer to the fuel jet axis, increasing the radial velocities through thermal expansion and accelerating the transition to the cone (lower S_C^*). The reduced viscosity associated with the lower adiabatic flame temperature leads to an enlarged unsteady conical breakdown with the flame sheet stabilized near the inlet

© 2022 The Author(s). Published by Elsevier Inc. on behalf of The Combustion Institute. This is an open access article under the CC BY license (http://creativecommons.org/licenses/by/4.0/)

Keywords: Vortex breakdown; Diffusion flame; Swirling jets

1. Introduction

Swirling jets are frequently used in combustion applications such as jet engines and gas turbines,

fast mixing near the inlet [1]. For sufficiently large values of the swirl number S, a measure of the ratio of circumferential to axial inlet velocity components, vortex breakdown, characterized by the formation of an internal stagnation point and a reversed axial flow [2], is known to occur. These recirculation regions serve as non-invasive flame-

where the entrainment of ambient fluid promotes

E-mail address: bwkeeton@ucsd.edu (B.W. Keeton).

https://doi.org/10.1016/j.proci.2022.07.013

 $15\dot{4}0\text{-}7489 © 2022 \text{ The Author(s)}. \text{ Published by Elsevier Inc. on behalf of The Combustion Institute. This is an open access article under the CC BY license (http://creativecommons.org/licenses/by/4.0/)}$

^{*} Corresponding author.

B.W. Keeton, K.K. Nomura, A.L. Sánchez et al. | Proceedings of the Combustion Institute xxx (xxxx) xxx

stabilizers, with the recirculating hot products promoting the reaction of the freshly injected reactants [3]. Previous vortex-breakdown studies, motivated by combustion applications, have addressed unconfined isothermal swirling jets in the turbulent regime [4,5], effects of heat release in confined premixed flames [6–9], and flame structure and behavior in nonpremixed configurations [10,11]. Despite these research efforts, our understanding of vortex breakdown in reactive swirling jets is still incomplete.

An aspect of the problem in need of further clarification pertains to the morphology of the flow emerging after breakdown. Previous experimental [12] and numerical [13] investigations of constantdensity flows have unveiled two primary forms of vortex breakdown in laminar swirling jets, namely, bubble breakdown and conical breakdown. As the swirl was increased from zero to a first critical swirl number, S_B^* , the slender pre-breakdown jet transitioned to bubble breakdown, identified by a stagnation point and reversed axial flow. As the swirl was increased further, the size of the bubble increased and the stagnation point moved upstream. Once the swirl reached a second critical swirl number, S_c^* , the bubble opened into a 90 degree conical sheet, and the pressure at the stagnation point jumped to the ambient value. These two types of breakdown have also been found to occur in hot and cold nonreacting gaseous swirling jets [14]. The corresponding reacting case, involving a laminar fuel jet discharging into an air atmosphere, is to be analyzed here in the Burke-Schumann limit of infinitely fast reaction for values of the thermochemical parameters corresponding to methane, with the Lewis numbers of fuel and oxidizer assumed to be unity, an excellent approximation for methane-air combustion. Conditions for existence of the different breakdown modes will be numerically investigated via axisymmetric unsteady solutions of the Navier-Stokes (NS) equations for different values of the fuel-jet dilution. As in previous investigations [12– 14], our jet-flame simulations will consider moderate values of the Reynolds number, for which the flow remains laminar and largely steady. Besides NS integrations, theoretical predictions for the onset of bubble breakdown will be obtained through the quasi-cylindrical (QC) approximation [15].

2. Formulation

2.1. The Burke-Schumann limit

The following study addresses jet diffusion flames formed by the discharge of a swirling fuel jet into a coaxial unconfined air stream. The mass fractions of fuel (Y_F) and oxygen (Y_{O_2}) take the values $Y_{F,j}$ and $Y_{O_2,A} = 0.23$ in their respective feed streams, with $Y_{F,j} < 1$ for configurations with fuelfeed dilution. For simplicity, the temperature of the

air stream will be assumed to be equal to the fuel-jet temperature T_i .

The description assumes that the fuel reacts with the oxygen of the air according to the overall irreversible reaction $F + s O_2 \rightarrow (1 + s) P + Q$, with P, s, and Q representing, respectively, the combustion products (carbon dioxide and water vapor), the mass of oxygen required to burn a unit mass of fuel, and the heat released per unit mass of fuel. To focus more directly on the fluid-mechanic aspects of the problem, the analysis considers the Burke-Schumann limit of infinitely fast reaction, in which the flame appears as an infinitesimally thin layer (a flame sheet) separating the fuel from the oxygen. The composition and temperature can be described in terms of coupling functions satisfying chemistryfree transport equations [16]. With the Lewis numbers of fuel and oxygen assumed to be unity, an excellent approximation for methane-air flames, the description reduces to a single scalar, the familiar mixture-fraction variable

$$Z = \frac{sY_{\rm F} - Y_{\rm O_2} + Y_{\rm O_2,A}}{sY_{\rm F,j} + Y_{\rm O_2,A}} = \frac{T - 1}{q} + \frac{Y_{\rm F}}{Y_{\rm F,j}},\tag{1}$$

which has been normalized to be unity in the fuel stream and zero in the air stream. In the formulation, T is the dimensionless temperature (scaled with T_j) and $q = (QY_{F,j})/(c_pT_j)$ is a dimensionless heat of reaction, with c_p representing the specific heat at constant pressure, assumed to be constant in the following description. At the flame, where $Y_F = Y_{O_2} = 0$, the mixture fraction takes the value

$$Z_s = \frac{1}{sY_{F,j}/Y_{O_2,A} + 1},$$
 (2)

while the temperature reaches its adiabatic value $T_s = 1 + \gamma$, with the parameter

$$\gamma = \frac{q}{sY_{F,j}/Y_{O_{2},A} + 1} \tag{3}$$

measuring the exothermicity of the reaction. Since $Y_F = 0$ on the air side, where $Z < Z_s$, while $Y_{O_2} = 0$ on the fuel side, where $Z > Z_s$, it follows from (1) that

$$T = 1 + \gamma \frac{Z}{Z_s} \qquad \text{for } Z \le Z_s \tag{4}$$

$$T = 1 + \gamma \frac{1 - Z}{1 - Z_s} \qquad \text{for } Z \ge Z_s. \tag{5}$$

For a given fuel-feed mass fraction $Y_{F,j}$, the thermochemical parameters Z_s and γ can be evaluated from (2), (3). For methane (i.e. s=4 and Q=50, 150 kJ/kg) with a feed temperature $T_j=300$ K and a presumed average specific heat $c_p=1.4$ kJ/(kg-K), it follows that $Z_s=(0.365,0.223,0.103,0.054)$ and $\gamma=(4.36,5.33,6.16,6.49)$ for values $Y_{F,j}=(0.1,0.2,0.5,1.0)$.

2.2. Governing equations

As in previous numerical studies [13,14], the analysis considers a fuel swirling jet of radius a and uniform velocity U_j undergoing solid-body rotation with angular speed Ω , with the associated swirl number defined as

$$S = \frac{\Omega a}{U_i}. (6)$$

The coaxial air stream, which is swirl free, has a small velocity ϵU_j , with $\epsilon \ll 1$. The jet radius a and jet velocity U_j will be used to scale the cylindrical coordinates $\mathbf{x} = (x, \theta, r)$ and accompanying velocity components $\mathbf{v} = (v_x, v_\theta, v_r)$. Correspondingly, the dimensionless time t is scaled with the residence time a/U_j . The fuel-jet values of the density ρ_j , viscosity μ_j , and thermal conductivity k_j will be used to define the dimensionless density ρ , viscosity μ , and thermal conductivity k, respectively. In terms of these variables, the non-dimensional NS equations, written in the low-Mach-number approximation, take the dimensionless form

$$\frac{\partial \rho}{\partial t} + \nabla \cdot (\rho \mathbf{v}) = 0 \tag{7}$$

$$\rho \left(\frac{\partial \mathbf{v}}{\partial t} + \mathbf{v} \cdot \nabla \mathbf{v} \right) = -\nabla p + \frac{1}{Re} \nabla \cdot \tau \tag{8}$$

$$\rho\left(\frac{\partial Z}{\partial t} + \mathbf{v} \cdot \nabla Z\right) = \frac{1}{Re \, Pr} \nabla \cdot (k \nabla Z),\tag{9}$$

where

$$Re = \frac{\rho_j U_j a}{\mu_i} \tag{10}$$

is the jet Reynolds number, $Pr = \mu_j c_p/k_j = 0.72$ is the Prandtl number evaluated in the fuel jet stream, $\tau = \mu [\nabla \mathbf{v} + \nabla \mathbf{v}^T - (2/3)\nabla \cdot \mathbf{v}\mathbf{I}]$ is the dimensionless viscous stress tensor, and p represents the pressure difference with respect to the ambient value, scaled with the characteristic dynamic pressure $\rho_j U_j^2$. Neglecting variations in the mean molecular weight, a reasonably good approximation for hydrocarbon combustion with air, the equation of state in the low-Mach-number limit takes the dimensionless form

$$\rho T = 1. \tag{11}$$

The viscosity and thermal conductivity are assumed to vary with temperature according to the power-law expressions

$$\mu = k = T^{\sigma},\tag{12}$$

with a value $\sigma = 0.7$ selected for the exponent, an appropriate value given the high concentration of air in the mixture.

2.3. Inlet boundary conditions

Following previous investigations of vortex breakdown in non-reacting jets [13,14], to facilitate computations smooth radial distributions of axial and azimuthal velocity components v_x and v_θ , given by the so-called Maxworthy profiles [17]

$$\frac{v_x - \epsilon}{1 - \epsilon} = \frac{v_\theta}{Sr} = \frac{1}{2} \operatorname{erfc}\left(\frac{r - 1}{\delta}\right), \quad v_r = 0, \tag{13}$$

are used at the inflow boundary x = 0, where the radial velocity v_r is set equal to zero. Here erfc is the complementary error function and δ represents the relative thickness of the mixing layer separating the jet from the coflow. For consistency, the same mixing-layer thickness δ is introduced in defining the associated mixture-fraction boundary profile

$$Z = \frac{1}{2} \operatorname{erfc}\left(\frac{r-1}{\delta}\right). \tag{14}$$

Note that the canonical case of a fuel jet with uniform velocity and solid-body rotation discharging into a stagnant air atmosphere is recovered from the above expressions by taking the limit $\epsilon \ll 1$ and $\delta \ll 1$. For sufficiently small values of these two parameters, the resulting variations in the values of the critical swirl numbers S_B^* and S_C^* are not very pronounced, as shown for nonreacting gaseous jets in Keeton et al. [14]. All simulations presented below employ $\delta = 0.2$ and $\epsilon = 0.01$. As discussed in previous numerical studies [13,14], effects of fixed inflow conditions may be important when vortex breakdown occurs in the vicinity of the inlet plane, but these effects are assumed negligible for the levels of inflow swirl considered here.

3. Numerical simulations

Numerical integrations of the unsteady axisymmetric NS Eqs. (7)–(9) were employed to characterize the onset of vortex breakdown and the morphology of the non-slender flow issuing after breakdown (i.e. for supercritical values of *S*).

3.1. Simulation description

The numerical integrations employed the highorder spectral element code Nek5000 [18] with $n_x \times n_r$ elements spanning a domain with $0 \le x \le x_{\max}$ and $0 \le r \le r_{\max}$. Calculations for the transition to the bubble employed a nonuniform grid with $(n_x, n_r) = (211, 34)$ spectral elements and $(x_{\max}, r_{\max}) = (100, 50)$, while simulations for the transition to the cone used $(n_x, n_r) = (211, 39)$ and $(x_{\max}, r_{\max}) = (100, 70)$. The fixed time-steps, $\Delta t = 5 \times 10^{-3}$ and $\Delta t = 2.5 \times 10^{-3}$, respectively, were selected to satisfy the Courant-Friedrichs— Lewy (CFL) condition. For both computational domains, the 7th order spectral elements were

Please cite this article as: B.W. Keeton, K.K. Nomura, A.L. Sánchez et al., Vortex breakdown in swirling Burke–Schumann flames, Proceedings of the Combustion Institute, https://doi.org/10.1016/j.proci.2022.07.013

3

JID: PROCI [mNS;July 22, 2022;20:25]

B.W. Keeton, K.K. Nomura, A.L. Sánchez et al. | Proceedings of the Combustion Institute xxx (xxxx) xxx

stretched to accommodate finer regions where the velocity and temperature gradients were large, which primarily occur at the reaction sheet. The axial and radial boundaries at x_{max} and r_{max} were placed sufficiently far away to avoid numerical contamination

Following previous numerical studies [19], to facilitate numerical convergence the piecewise linear relations (4) and (5) were replaced in the calculations by a smooth functional relation involving a hyperbolic tangent profile, thereby avoiding discontinuities in the gradients of density and temperature.

The profiles of velocity and mixture fraction (13) and (14) were prescribed at the inflow plane x = 0. Stress-free adiabatic conditions $-p\mathbf{e}_r + \mathbf{e}_r \cdot \left[\mu(\nabla \mathbf{v} + \nabla \mathbf{v}^T)/Re\right] = 0$ and $\mathbf{e}_r \cdot \nabla Z = \partial Z/\partial r = 0$ were applied on the lateral boundary $r = r_{\text{max}}$, with \mathbf{e}_r representing the unit vector in the radial direction. At the outflow plane $x = x_{\text{max}}$, a convective condition was applied to the velocity and mixture fraction [17].

Following [13,14], the transient numerical integrations were initialized at t = 0 using as an initial condition at all x the velocity and mixture-fraction radial distributions given by the inlet boundary profiles (13) and (14). To identify each critical swirl number, simulations were conducted in increasing increments of $\Delta S = 0.01$ for a given set of γ and Z_s . Except for $(Y_{F,j}, S) = (0.1, S_c^*)$, to be discussed below, all flows reached a statistically steady state characterized by changes in the axial velocity smaller than 7.5×10^{-3} over a duration of $\Delta t =$ 250. The transition to bubble breakdown at S_B^* was distinguished from the pre-breakdown state by the appearance of a stagnation point at the axis. The transition to the cone at S_C^* was identified by a sudden increase in the pressure along the jet centerline to the ambient value $(-4 \times 10^{-3} \le p \le 0)$. As S was increased by 0.01, all transitions at S_C^* exceeded a 76% increase in the pressure at the first stagnation point (see Fig. 3(b), to be discussed later).

Code validation for the isothermal flow has previously been performed [14]. To validate the Burke–Schumann problem, we conducted simulations of zero-swirl jet diffusion flames in the absence of gravity, and found good agreement between the calculated flame heights and those measured in previous experiments [20].

3.2. Vortex breakdown modes

The evolution of the flow morphology for increasing swirl levels depends on the fuel dilution, as shown in the selected sample computations displayed in Figs. 1, 2 and 4 for Re = 800. In these figures, the black lines represent the streamlines projected onto the meridional plane, the yellow curve is the reaction sheet $Z = Z_s$, and the color contours denote the temperature $1 \le T \le 1 + \gamma$. Corresponding values of S_B^* and S_C^* are compared in

Table 1 Critical swirl numbers for various values of fuel-feed mass fraction at Re = 800.

$Y_{\mathrm{F},j}$	QC	S_B^*	S_C^*
0.1	1.338	1.36	1.80
0.2	1.339	1.36	1.83
0.5	1.339	1.36	1.83
1.0	1.339	1.36	1.83

Table 1 with the QC predictions, to be discussed below.

Figs. 1 and 2, corresponding to $Y_{F,j} = 0.2$, illustrate the typical transition pattern observed for moderate values of the dilution ($Y_{F,j} \ge 0.2$). Note that the plots in Figs. 1, 2 and 4 are scaled differently due to the difference in spatial extent of each transition. The flow, which remains slender for $S \leq 1.35$, with streamlines aligned with the axis shown in the top panel of Fig. 1, displays for S = $S_B^* = 1.36$ the formation of a two-celled recirculation bubble of transverse size comparable to the jet radius. The reaction sheet is deflected by and passes over the recirculating fuel and products, creating a jet-like flame that lies at radial distances from the axis that are slightly larger than the pre-breakdown case S = 1.35. In both cases, the flame sheet eventually closes on the axis far downstream.

As S is increased beyond $S_B^* = 1.36$ (Fig. 2), the swirl-induced adverse pressure gradient increases and the steady two-celled bubble continuously grows in size. The enhanced scalar transport with increasing S results in reduced values of the mixture fraction within the jet and a corresponding reduction in flame length. At $S = S_C^* = 1.83$, a second abrupt transition occurs leading to the formation of a steady compact one-celled cone, shown in the bottom panel of Fig. 2.

During this transition, the flow opens and the pressure along the centerline jumps to the ambient value, as shown in Fig. 3(b). The negative axial velocities, shown in Fig. 3(a), continue further downstream, corresponding to the single large cell which recirculates hot products, increasing the temperature inside the breakdown region. The flame sheet, however, again passes around the recirculation region similar to the bubble, maintaining a jet-like flame. A similar two-stage transition is observed for $Y_{{\rm F},j} \geq 0.2$ (not shown).

The most diluted jet, corresponding to $Y_{F,j} = 0.1$, exhibits similar behavior for $S < S_C^*$ as described above. However, a transition to an unsteady cone occurs at $S_C^* = 1.80$, with corresponding time-averaged streamlines shown in the bottom panel of Fig. 4, and instantaneous fields in Fig. 5. A temporal average of 41 instantaneous fields spanning the interval 38, $000 \le t \le 40$, 000 was sufficient for determining the average behavior. For this small value of $Y_{F,j}$, Z_s is large, moving the reaction sheet inward closer to the jet axis. The viscosity is reduced

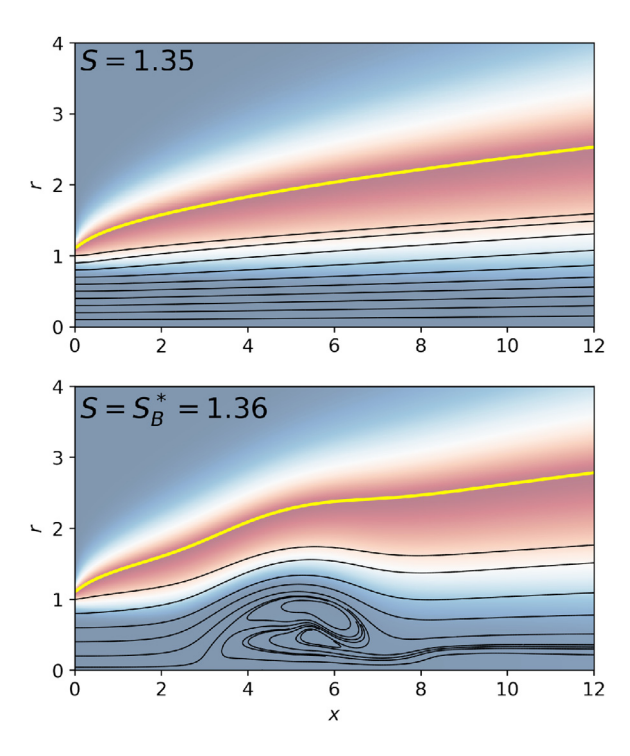


Fig. 1. Projected streamlines superimposed on color contours of temperature before and at the transition to the bubble for $Y_{F,j} = 0.2$ and Re = 800.

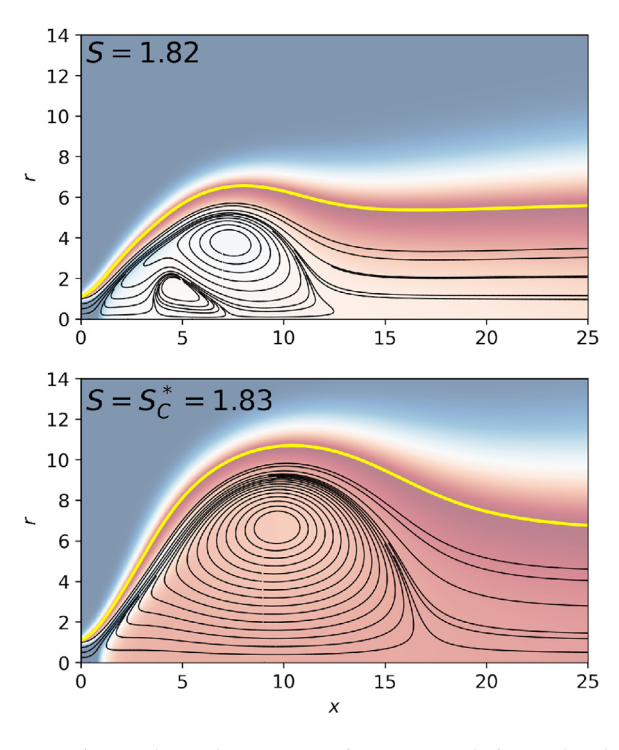


Fig. 2. Projected streamlines superimposed on color contours of temperature before and at the transition to the cone for $Y_{F,j} = 0.2$ and Re = 800.

6 B.W. Keeton, K.K. Nomura, A.L. Sánchez et al. | Proceedings of the Combustion Institute xxx (xxxx) xxx

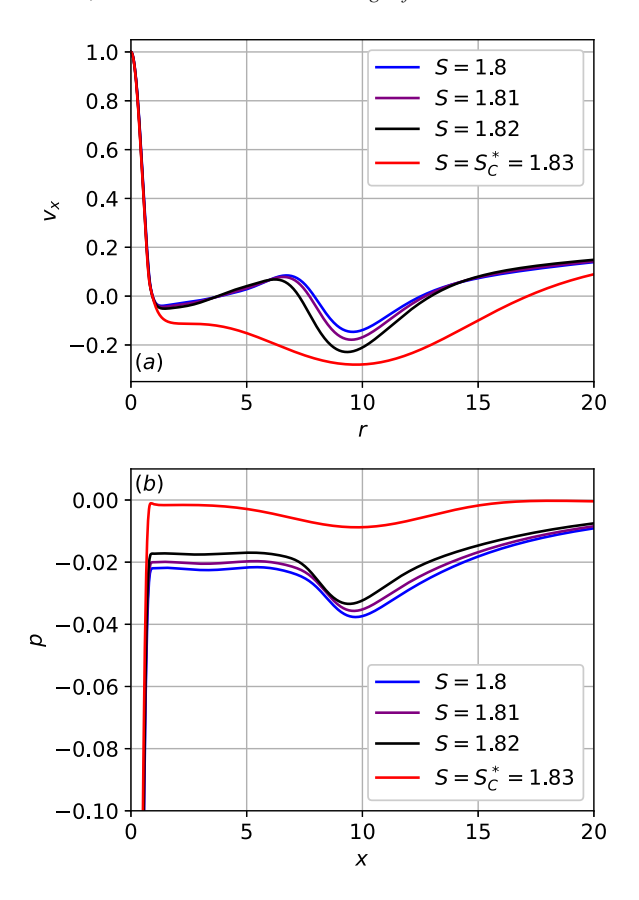


Fig. 3. Plots of (a) centerline axial velocity and (b) centerline pressure before and at the transition to the cone for $Y_{F,j} = 0.2$ and Re = 800.

because of the small value of γ (4.36), and the recirculation region becomes unstable, opening into an enlarged unsteady cone, a state also found for cold variable-density jets [14]. The unsteady nature of the flow is shown in the instantaneous temperature contours in Fig. 5, where vortex shedding modes persist in the far-field. The resulting flame shape, which is relatively fixed in time (see inset in bottom plot of Fig. 4 and Fig. 5), is no longer jet-like, but is confined close to the inlet and surrounds the fixed portion of the conical sheet. As discussed earlier, enhanced mixing with increased S causes the flame length to decrease. For $Y_{F,j} = 0.1$, the larger value of Z_s causes the flame sheet to move into the recirculation region during the transition, and eventually stabilize along the cone. The resulting recirculation cell now extends further out and entrains fresh air that feeds the rear surface of the flame stabilized near the inlet.

3.3. Effects of thermochemical parameters

As discussed earlier, for increasing dilution of the fuel jet (decreasing values of $Y_{F,j}$), Z_s increases and γ decreases. To identify the independent ef-

Table 2 Critical swirl numbers for various values of thermochemical parameters at Re = 800.

γ	Z_s	QC	S_B^*	S_C^*
4.36	0.223	1.332	1.35	1.83
5.33	0.223	1.339	1.36	1.83
6.49	0.223	1.347	1.38	1.82
5.33	0.054	1.332	1.35	1.83
5.33	0.223	1.339	1.36	1.83
5.33	0.365	1.346	1.38	1.80

fects of Z_s and γ , critical swirl numbers were calculated after modifying one of these parameters, holding the other fixed, and the results were compared to the reference case $Y_{F,j} = 0.2$ ($\gamma = 5.33$, $Z_s = 0.223$) in Table 2, which also includes predictions obtained using the quasi-cylindrical approximation, to be discussed later.

Increasing γ delays the transition to the bubble through the increased viscosity, resulting in a higher S_B^* . This trend is consistent with previous computations of constant-density [21] and variable-density [14] jets, where values of S_B^* were

Fig. 4. Time-averaged projected streamlines superimposed on color contours of temperature before and at the transition to the cone for $Y_{F,j} = 0.1$ and Re = 800.

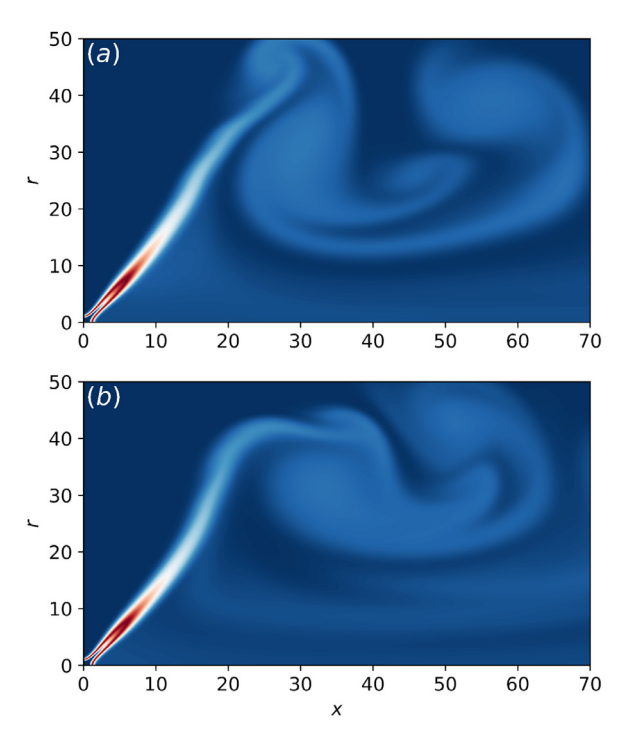


Fig. 5. Instantaneous color contours of temperature for $S = S_C^* = 1.80$, $Y_{F,j} = 0.1$ and Re = 800 at (a) t = 39,000 and (b) t = 40,000.

Please cite this article as: B.W. Keeton, K.K. Nomura, A.L. Sánchez et al., Vortex breakdown in swirling Burke-Schumann flames, Proceedings of the Combustion Institute, https://doi.org/10.1016/j.proci.2022.07.013

JID: PROCI [mNS; July 22, 2022; 20:25]

B.W. Keeton, K.K. Nomura, A.L. Sánchez et al. | Proceedings of the Combustion Institute xxx (xxxx) xxx

found to increase for decreasing values of the Reynolds number. The physical mechanism for this trend will be elaborated in the following subsection. Although viscous effects increase with higher γ , the transition to the cone is promoted (i.e. smaller S_C^*). This can be explained by noting that, unlike the previous investigations of constant-density and variable-density jets [14], the velocity divergence $\nabla \cdot \mathbf{v} = \nabla \cdot (k \nabla T)/(Re \, Pr)$ is non-negligible in the reactive case, and increases in magnitude for larger values of γ . The increased positive radial velocities inside the flame envelope, associated with this thermal expansion, enlarge the bubble's recirculation zone, leading to lower values of S_C^* .

As Z_s decreases, the reaction sheet is positioned at larger radial distances from the axis, decreasing the temperature in the mixing layer and increasing the centerline adverse axial pressure gradient, lowering S_B^* . Increases in Z_s move the reaction sheet radially inward, increasing the temperature in the recirculation region and decreasing S_c^* .

The counteracting effects of changes in Z_s and γ for changes in $Y_{F,j}$ lead to the constant values S_B^* in Table 1. For the transition to the cone, the effects from the decrease in Z_s outweigh the effects of increasing γ as $Y_{F,j}$ increases from 0.1 to 0.2, raising S_C^* . For further decrease in dilution in the range $0.2 \le Y_{F,j} \le 1$, the decrease in Z_s is small, and the increase in γ balances these effects, leading to constant values S_C^* .

3.4. Effects of Reynolds number

Critical swirl numbers were calculated for increasing Re for $Y_{F,j} = 0.2$. For Re = (800, 1000), it is found that $S_B^* = (1.36, 1.35)$ and $S_C^* = (1.83, 1.81)$, indicating that the small increase in the Reynolds number slightly decreases both critical swirl numbers. At the moderately low Reynolds numbers considered, increases in Re decrease the viscous damping effects on the wave motions associated with the formation of bubble breakdown, decreasing S_R^* . This result is consistent with previous experimental studies on isothermal breakdown for which S_B^* decreased for increasing Re up to a critical value, above which S_R^* remained constant [22]. This effect also leads to an increase in the overshoot of the initial divergence of the streamlines (Fig. 6), increasing the size of the bubble, and promoting the jump to the cone (lower S_C^*). While variation in both critical swirl numbers is small in the range $800 \le Re \le 1000$, the effect on the flow, illustrated in Fig. 6, is more pronounced, and the enlarged breakdown of the higher Re bubble considerably increases the temperature along the jet axis. The decrease in both S_R^* and S_C^* for increasing Re has also been observed in previous work on non-reacting gaseous jets [14].

4. Quasi-cylindrical approximation

4.1. Problem formulation

One of the classical approaches to the computation of vortex breakdown, originally proposed by Hall [15], involves the so-called quasi-cylindrical (OC) approximation of viscous axisymmetric flow. For moderately large values of Re, in the absence of vortex breakdown the jet remains slender, so that the axial variations of velocity, temperature and composition are small compared to those in the radial direction. This slender flow includes a development region $x \sim Re$ where the axial velocity v_x is of order unity and the radial velocity v_r is of order $Re^{-1} \ll 1$. Introducing the dimensionless circulation per unit azimuthal angle $\Gamma = rv_{\theta}/S$, rescaled axial distance $\hat{x} = x/Re$ and rescaled radial velocity $\hat{v}_r = Re v_r$ and neglecting small terms of order Re^{-2} leads to the QC equations

$$\frac{\partial}{\partial \hat{x}}(\rho v_x) + \frac{1}{r} \frac{\partial}{\partial r}(\rho r \hat{v}_r) = 0, \tag{15}$$

$$\rho \left(v_x \frac{\partial v_x}{\partial \hat{x}} + \hat{v}_r \frac{\partial v_x}{\partial r} \right) = -\frac{\partial p}{\partial \hat{x}} + \frac{1}{r} \frac{\partial}{\partial r} \left(\mu r \frac{\partial v_x}{\partial r} \right), \tag{16}$$

$$0 = S^2 \rho \frac{\Gamma^2}{r^3} - \frac{\partial p}{\partial r},\tag{17}$$

$$\rho \left(v_x \frac{\partial \Gamma}{\partial \hat{x}} + \hat{v}_r \frac{\partial \Gamma}{\partial r} \right) = \frac{1}{r} \frac{\partial}{\partial r} \left(\mu r \frac{\partial \Gamma}{\partial r} - 2\mu \Gamma \right)$$
 (18)

$$\rho\left(v_{x}\frac{\partial Z}{\partial \hat{x}} + \hat{v}_{r}\frac{\partial Z}{\partial r}\right) = \frac{1}{r}\frac{\partial}{\partial r}\left(\frac{k}{\Pr}r\frac{\partial Z}{\partial r}\right),\tag{19}$$

to be integrated with inlet boundary conditions at $\hat{x} = 0$ given in (13) and (14), radial boundary conditions

$$v_x - \epsilon = \Gamma = Z = 0 \quad \text{as} \quad r \to \infty,$$
 (20)

and regularity conditions

$$\frac{\partial v_x}{\partial r} = \hat{v}_r = \Gamma = \frac{\partial Z}{\partial r} = 0$$
 at $r = 0$. (21)

This parabolic problem, independent of Re, can be integrated by marching downstream in the axial direction, as done previously for isothermal [23], compressible [24] and non-isothermal gaseous [14] swirling jets. As reasoned by Hall [15], if in the course of the integration for a given value of S the solution develops a singularity at a given location, characterized by a rapid increase of axial gradients and radial velocities, there must also be appreciable axial gradients at that location in the associated real vortex core, corresponding to vortex breakdown. The appearance of this singularity has been shown to identify the onset of bubble breakdown [14], so that the critical value of S at failure corresponds to S_B^* .

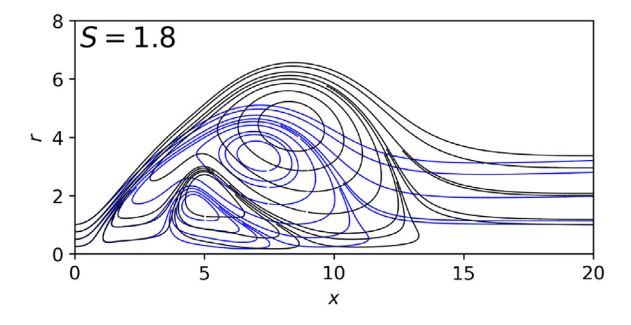


Fig. 6. Projected streamlines for bubble breakdown at $Y_{F,j} = 0.2$ and Re = 800 (blue) and Re = 1000 (black). (For interpretation of the references to color in this figure legend, the reader is referred to the web version of this article.)

4.2. Numerical method

The integration of (13)–(21) employs a first/second order discretization of the axial/radial derivatives. The implicit integration in the axial direction begins with the inlet boundary conditions (13) and (14) at $\hat{x} = 0$. At each axial location, Newton's method is first used to determine v_x and \hat{v}_r from (15), (16). Next, the boundary value problems given by (18) and (19) are solved for the circulation and mixture fraction, and the radial distribution of pressure is updated through (17). The temperature, density and viscosity are calculated through (4), (5), (11) and (12), respectively, and a fixed point iteration method is used until the solution at the given axial location converges. The integration then moves to the next axial location, and repeats the same process. The finite difference grid uses spacing $\delta \hat{x} = 5 \times 10^{-5}$ and $\delta r = 10^{-3}$, and integrations were carried out to an axial distance $\hat{x}_{\text{max}} = 0.1$. In the radial direction, the $r \to \infty$ conditions are applied at a truncated boundary placed at $r_{\text{max}} = 15$. Tests were conducted with the radial boundary extended to $r_{\text{max}} = 50$, and critical swirl numbers were found to be identical. To obtain the critical swirl numbers, subsequent integrations were performed in increasing increments of $\Delta S = 0.001$ until the singularity was detected.

4.3. QC predictions

The quasi-cylindrical integrations were carried out using the same values of the thermochemical parameters Z_s and γ as the Navier–Stokes simulations. Fuel dilution was found to have a negligible effect on breakdown, in that for all values of dilution considered the numerical integration failed at a nearly constant value of S_B^* in the range 1.338 $\leq S_B^* \leq 1.339$, as shown in Table 1, with the singularity developing at axial locations in the narrow range $0.016 < \hat{x} < 0.0172$. Additional integrations for other values of the thermochemical parameters, reported in Table 2, showed also minute changes in resulting values of S_B^* .

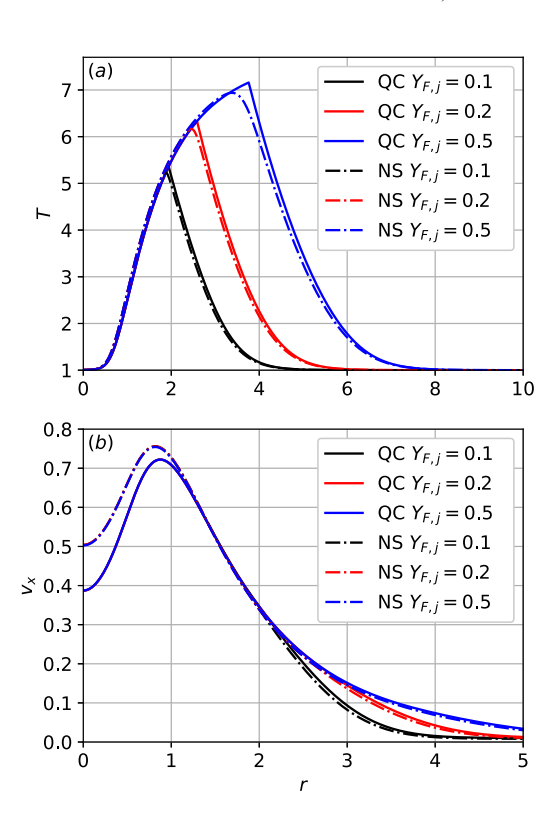


Fig. 7. Comparison of temperature and axial velocity profiles at $\hat{x} = 0.015$ for S = 1.3 and Re = 1000 and various values of $Y_{\rm F, i}$.

To explain the lack of influence of the dilution on the QC predictions, radial distributions of temperature and axial velocity corresponding to the near-critical case S=1.3 are shown in Fig. 7 for different values of $Y_{F,j}$. As can be seen, fuel-feed dilution results in significant changes of the temperature across the envelope of hot products and air that surrounds the flame, while the interior structure of the jet extending extending radially from the axis to the flame remains unperturbed. Since the singularity of the QC integrations develops near

JID: PROCI [mNS;July 22, 2022;20:25]

10 B.W. Keeton, K.K. Nomura, A.L. Sánchez et al. | Proceedings of the Combustion Institute xxx (xxxx) xxx

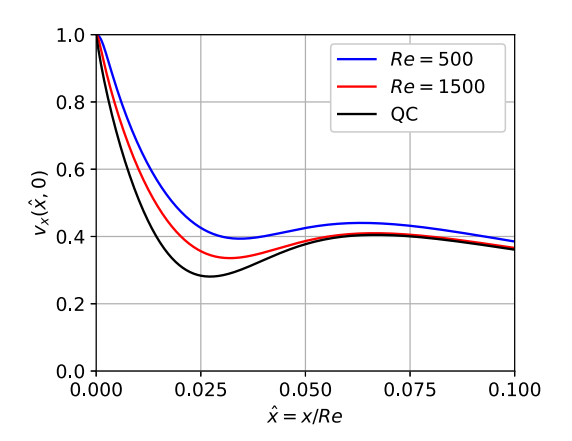


Fig. 8. The distribution of axial velocity at r = 0 obtained from the QC approximation and the NS simulations for S = 1.3 and $Y_{F,j} = 0.2$.

the axis, where the flow is independent of $Y_{F,j}$, the resulting values of S_B^* are nearly identical in all cases.

4.4. Comparisons between QC and NS results

According to the reasoning used in the derivation of (15)–(19), for slender flows with $S < S_B^*$ the results of the NS integrations should approach for $Re \gg 1$ those of the QC approximation. To test this premise, centerline axial velocities obtained from the unsteady NS simulations for a near-breakdown swirl level ($S = 1.3 < S_B^*$) are compared to those determined with the QC approximation in Fig. 8. As the Reynolds number is increased, the slender flow approximation improves, and the Navier-Stokes solutions converge towards the QC prediction. The radial distributions of the NS solutions at an axial location just before breakdown are also in excellent agreement with the QC results (Fig. 7), except for the slight increase in the jet core axial velocity due to the moderately low Re. Thus, the QC approximation provides an excellent description of the slender pre-breakdown flow and the transition to the bubble S_R^* .

5. Conclusions

Unsteady Navier–Stokes simulations have been used to identify the transition to bubble and conical vortex breakdown in unconfined laminar swirling Burke–Schumann flames. For the hydrocarbon flames considered, critical swirl numbers for both the bubble and cone remain relatively constant across a wide range of dilution. Two different forms of the conical breakdown flame were identified. For more realistic values of dilution, a steady compact cone is found with a flame sheet that passes around the recirculation region, forming a jet-like flame.

For extreme dilution, an enlarged unsteady cone formed with a recirculation region that stabilizes the flame sheet near the jet inlet. In both cases, the transition from the bubble to the cone leads to increased recirculation of combustion products that considerably increases the temperature within the breakdown region. The Reynolds numbers considered are moderate so that the flow is stable and axisymmetric, but the high Reynolds numbers used in practical combustors warrant future study of the effects of turbulence on the flame transitions and morphology.

Declaration of Competing Interest

The authors declare that they have no known competing financial interests or personal relationships that could have appeared to influence the work reported in this paper.

Acknowledgments

Computational resources for the unsteady NS simulations were provided by XSEDE [25]. The work of ALS was supported by the US National Science Foundation through grant # 1916979.

References

- [1] N. Syred, J. Beer, Combustion in swirling flows: a review, Combust. Flame 23 (2) (1974) 143–201.
- [2] S. Leibovich, The structure of vortex breakdown, Annu. Rev. Fluid Mech. 10 (1) (1978) 221–246.
- [3] S. Candel, D. Durox, T. Schuller, J.-F. Bourgouin, J.P. Moeck, Dynamics of swirling flames, Annu. Rev. Fluid Mech. 46 (1) (2014) 147–173.
- [4] S. Farokhi, R. Taghavi, E.J. Rice, Effect of initial swirl distribution on the evolution of a turbulentjet, AIAA J. 27 (6) (1989) 700–706.
- [5] K. Oberleithner, C. Paschereit, R. Seele, I. Wygnanski, Formation of turbulent vortex breakdown: intermittency, criticality, and global instability, AIAA J. 50 (7) (2012) 1437–1452.
- [6] Z. Rusak, A. Kapila, J. Choi, Effect of combustion on near-critical swirling flow, Combust. Theory Model. 6 (4) (2002) 625.
- [7] Z. Rusak, J. Choi, N. Bourquard, S. Wang, Vortex breakdown in premixed reacting flows with swirl in a finite-length circular open pipe, J. Fluid Mech. 793 (2016) 749–776.
- [8] C. Umeh, Z. Rusak, E. Gutmark, Vortex breakdown in a swirl-stabilized combustor, J. Propul. Power 28 (5) (2012) 1037–1051.
- [9] J. Choi, Z. Rusak, A. Kapila, Numerical simulation of premixed chemical reactions with swirl, Combust. Theor. Model. 11 (6) (2007) 863–887.
- [10] V. Tangirala, J. Driscoll, Temperatures within non-premixed flames: effects of rapid mixing due to swirl, Combust. Sci. Technol. 60 (1–3) (1988) 143–162.

ARTICLE IN PRESS [mNS;July 22, 2022;20:25]

B.W. Keeton, K.K. Nomura, A.L. Sánchez et al. | Proceedings of the Combustion Institute xxx (xxxx) xxx

[11] R. Santhosh, S. Basu, Transitions and blowoff of unconfined non-premixed swirling flame, Combust. Flame 164 (2016) 35–52.

JID: PROCI

- [12] P. Billant, J.-M. Chomaz, P. Huerre, Experimental study of vortex breakdown in swirling jets, J. Fluid Mech. 376 (1998) 183–219.
- [13] P. Moise, J. Mathew, Bubble and conical forms of vortex breakdown in swirling jets, J. Fluid Mech. 873 (2019) 322–357.
- [14] B.W. Keeton, J. Carpio, K.K. Nomura, A.L. Sánchez, F.A. Williams, Vortex breakdown in variable-density gaseous swirling jets, J. Fluid Mech. 936 (2022) A1.
- [15] M.G. Hall, A new approach to vortex breakdown, in: Proceedings of Heat Transfer and Fluid Mechanics Institute, Stanford University Press, 1967, pp. 319–340.
- [16] A. Liñán, M. Vera, A.L. Sánchez, Ignition, liftoff, and extinction of gaseous diffusion flames, Annu. Rev. Fluid Mech. 47 (2015) 293–314.
- [17] M.R. Ruith, P. Chen, E. Meiburg, Development of boundary conditions for direct numerical simulations of three-dimensional vortex breakdown phenomena in semi-infinite domains, Comput. Fluids 33 (9) (2004) 1225–1250.
- [18] P. Fischer, J. Lottes, S. Kerkemeier, nek5000 web page, 2008. http://nek5000.mcs.anl.gov.

- [19] F. Higuera, R. Moser, Effect of chemical heat release in a temporally evolving mixing layer, in: CTR Report, 1994, pp. 19–40.
- [20] J. Haggard Jr, T. Cochran, Stable hydrocarbon diffusion flames in a weightless environment, Combust. Sci. Tech. 5 (1) (1972) 291–298.
- [21] P. Moise, J. Mathew, Hysteresis and turbulent vortex breakdown in transitional swirling jets, J. Fluid Mech. 915 (2021) A94.
- [22] R. Spall, T. Gatski, C. Grosch, A criterion for vortex breakdown, Phys. Fluids 30 (11) (1987) 3434–3440.
- [23] A. Revuelta, A.L. Sánchez, A. Liñán, The quasicylindrical description of submerged laminar swirling jets, Phys. Fluids 16 (3) (2004) 848–851.
- [24] J.M. Gallardo-Ruiz, C. del Pino, R. Fernandez-Feria, Quasicylindrical description of a swirling light gas jet discharging into a heavier ambient gas, Phys. Fluids 22 (11) (2010) 113601.
- [25] J. Towns, T. Cockerill, M. Dahan, I. Foster, K. Gaither, A. Grimshaw, V. Hazlewood, S. Lathrop, D. Lifka, G.D. Peterson, R. Roskies, J. Scott, N. Wilkins-Diehr, Xsede: accelerating scientific discovery, Comput. Sci. Eng. 16 (05) (2014) 62–74, doi:10.1109/MCSE.2014.80.

11